INORGANIC CHEMISTRY FRONTIERS

RESEARCH ARTICLE

Published on 22 June 2026

Cite this: DOI: 10.1039/d6qi01087c

Exchange-transferred anisotropy: an isotropic Mn^{II} ion governs single-molecule magnetism in a $\{Mn_9\}$ double-decker metallacrown

Konstantina H. Baka,[a] Max Kallio,[b] Veacheslav Vieru,[b] Andrew M. Mowson,[c] Evangelia S. Koumousi,[a] Catherine P. Raptopoulou,[d] Vassilis Psycharis,[d] Wolfgang Wernsdorfer,[e,f] Eufemio Moreno-Pineda,[f,g,h] George Christou,[c] Liviu F. Chibotaru *[i] and Theocharis C. Stamatatos *[a]

A mixed-valence $\{Mn^{II}Mn^{III}_8\}$ (**1**) cluster with a double-decker structure comprising a central eight-coordinate Mn^{II} atom surrounded by a coupled array of eight five-coordinate Mn^{III} atoms was isolated. Magnetic measurements revealed an S = 5/2 spin ground state associated with a large molecular D value of −2.5 cm^{-1}. Complex **1** behaves as a single-molecule magnet (SMM) exhibiting entirely visible out-of-phase magnetic susceptibility signals (χ''_M) and open hysteresis loops below 2 K, with an effective energy barrier for the magnetization reversal of 16.6 K. Computational analysis uncovers the origin of the unexpectedly strong magnetic anisotropy of the central Mn^{II} ion in complex **1**, revealing that it emerges from a synergistic interplay between the pronounced axial anisotropy of the surrounding Mn^{III} ions and the substantial exchange coupling that links them. To the best of our knowledge, this represents the first example where an isotropic ion (Mn^{II}) effectively controls the SMM behavior of the entire cluster. This counterintuitive phenomenon arises only when three stringent conditions are simultaneously satisfied: (i) a high density of strongly anisotropic magnetic neighbors, (ii) efficient magnetic communication through relatively strong antiferromagnetic exchange interactions, and (iii) a geometric arrangement that maximizes anisotropy transfer to the isotropic center.

Received 18th May 2026,
Accepted 22nd June 2026

DOI: 10.1039/d6qi01087c

rsc.li/frontiers-inorganic

Introduction

Polynuclear Werner-type complexes (or coordination clusters) of metal ions in moderate oxidation states (*i.e.*, +2 and +3) provide a meaningful molecular platform for the study of several exciting physical phenomena, such as magnetic, quantum, optical, and catalytic.[1] Single-molecule magnets (SMMs) are coordination compounds that, below a critical (blocking) temperature, retain their magnetization upon the removal of an external magnetic field,[2] and they are considered powerful precursors for the development of materials with multiple properties, such as magnetic/quantum,[3,4] magneto-optical,[5] and magnetic/conductive,[6] either in their single-molecule phase[7] or as a part of a hybrid material (*i.e.*, deposited on graphene substrates,[8–10] anchored to gold surfaces,[11] *etc.*). The abundance of first-row transition metals in Earth's upper continental crust, such as Mn and Fe, has made these elements attractive for the preparation of sustainable magnetic materials.

Mn^{III}-containing complexes stabilized by a sheath of organic ligands have been central to the field of SMMs for over two decades.[12] However, recent advances have highlighted the enhanced magnetic dynamics of oligonuclear 4f-metal complexes. This improvement arises from their significant magnetic anisotropy, which is induced by strong intrinsic spin–orbit coupling in the presence of an appropriate ligand field.[13–15] Organic ligands of various donor atoms, such as

[a]*Department of Chemistry, University of Patras, 265 04 Patras, Greece. E-mail: thstama@upatras.gr*
[b]*Maastricht Science Programme, Faculty of Science and Engineering, Maastricht University, 6229 GS Maastricht, The Netherlands*
[c]*Department of Chemistry, University of Florida, Gainesville, 32611-7200 Florida, USA*
[d]*Institute of Nanoscience and Nanotechnology, NCSR "Demokritos", Aghia Paraskevi Attikis 15310, Greece*
[e]*Physikalisches Institut, Karlsruhe Institute of Technology (KIT), Kaiserstraße 12, Karlsruhe, D-76131, Germany*
[f]*Institute for Quantum Materials and Technology (IQMT), Karlsruhe Institute of Technology (KIT), Hermann-von-Helmholtz-Platz 1, Eggenstein-Leopoldshafen, D-76344, Germany*
[g]*Facultad de Ciencias Naturales, Exactas y Tecnología, Depto. de Química-Física, Universidad de Panamá, 0824 Panamá, Panamá*
[h]*Facultad de Ciencias Naturales, Exactas y Tecnología, Grupo de Investigación de Materiales, Universidad de Panamá, 0824 Panamá, Panamá*
[i]*Theory of Nanomaterials Group, Katholieke Universiteit Leuven, Celestijnenlaan 200F, Leuven, B-3001, Belgium. E-mail: liviu.chibotaru@gmail.com*

carboxylate ions,[16,17] polyalcohols,[18,19] oximes[20–23] and hydroxamic acids,[24,25] have provided an invaluable playground for the synthesis of aesthetically pleasing polynuclear Mn^{III}-based SMMs with large ground state spin values, S,[26–29] remarkable energy barriers for magnetization reversal,[30,31] and exotic quantum phenomena, such as quantum tunneling of magnetization,[32] quantum phase interference,[33] and quantum coherence.[34] Magnetic anisotropy, as reflected in a large and negative zero-field splitting parameter, D, constitutes one of the most impactful factors for the preparation of highly effective 3d-metal SMMs.[35–38] Concurrently though, molecular magnetic anisotropy depends on the overall topology of the compound and the geometrical constraints and electronic properties of the individual metal ions, thus making the synthesis of highly anisotropic 3d-metal clusters a very challenging task.

Indeed, several years ago, Waldmann reported calculations that led to the conclusion that for a better performing 3d-metal based SMM with a large anisotropy barrier, U, it would be more promising to increase D rather than the S of a cluster compound because increasing S is not as efficient as suggested by $U = S^2|D|$, *i.e.*, that the increase in U is on the order of unity and not S^2.[39] Experimentally, this turned out to be the case in many polynuclear Mn-based SMMs of different nuclearities and metal topologies.[40–43] Among all of them, clusters with 'magical' S values of 10–12 appeared to exhibit appreciable D values in the −0.38 to −0.50 cm^{-1} range, resulting in groundbreaking SMMs with record barriers and magnetization hysteresis loops up to 4 K.[44–46] Since the golden era of the $\{Mn_{12}\}$/carboxylate[47] and $\{Mn_6\}$/oximate families of SMMs,[48] and more recently the giant $\{Mn_{31}\}$ nanosized SMM,[49] the interest has shifted to increasing the record of energy barriers in lanthanide molecular nanomagnets; this has led to myriads of high-performance SMMs,[50–52] albeit only a few air-stable, non-organometallic compounds with open hysteresis in zero field.[53–56]

Exploiting the great coordination capabilities of salicylhydroxamic acid ($shaH_2$, Scheme 1) and its amide–iminol tautomeric form (salicylhydroxime, $shiH_3$, Scheme 1), Pecoraro and co-workers have contributed significantly to the development of metallacrown-based SMMs using either pure homometallic 3d-metal complexes or heterometallic 3d/3d′ and 3d/4f systems.[57,58] In 2011, the pentanuclear $[Mn^{II}Mn^{III}_4(O_2CMe)_2(shi)_4(DMF)_6]$ metallacrown consisting of a $\{Mn^{III}_4\}$-salicylhydroximate square base bridged to an apical Mn^{II} atom through acetate groups was reported.[59] The four Mn^{III} atoms were antiferromagnetically coupled yielding a local $S = 0$, while the overall spin ground state of the system was determined by the trigonal prismatic Mn^{II} atom with spin $S = \frac{1}{2}$. Interestingly, the $\{Mn^{III}_4–Mn^{II}\}$ single-decker compound exhibited a quite large $D_{Mn(III)}$ value of ∼−3.0 cm^{-1} and, regardless of its very small S, it behaved as an SMM below a very low temperature of 0.04 K.

We herein report the synthesis of a new $\{Mn^{III}_4–Mn^{II}–Mn^{III}_4\}$ double-decker SMM, resulting from two $\{Mn^{III}_4Mn^{II}\}$-salicylhydroximate square pyramidal units that share a common, eight-coordinate Mn^{II} atom. The complex $(Et_2NH_2)_2[Mn^{II}Mn^{III}_8(OH)_4(shi)_8]$ (**1**) exhibits an S = 5/2 spin ground state and a large D value of −2.5 cm^{-1}, making it the smallest spin and highest anisotropy 3d-metal cluster SMM reported to date with open hysteresis at temperatures below 2.0 K. For the first time in 3d-metal cluster chemistry, computational studies show that while the net magnetic moment at low temperature is dominated by the Mn^{II} ion (effective S = 5/2 description), the Mn^{III} ions play a crucial indirect role by transferring their large single-ion anisotropy to the Mn^{II} center through exchange coupling. This mechanism is demonstrated quantitatively by *ab initio* calculations, which show that the intrinsic zero-field splitting (ZFS) of Mn^{II} is negligible, whereas inclusion of exchange and Mn^{III} axial anisotropy produces a ZFS of a large order of magnitude.

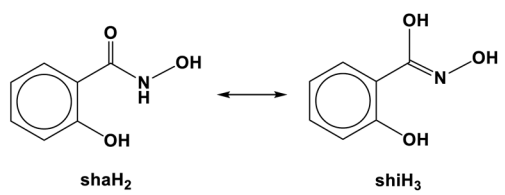

Scheme 1 Structures and abbreviations of the organic ligands employed in this study.

Results and discussion

Materials and methods

Aerobic conditions were applied to all manipulations using materials (reagent grade) and solvents as received. No uncommon hazards were noted.

Synthesis of $(Et_2NH_2)_2[Mn_9(OH)_4(shi)_8]·3.3MeCN·MeOH$ (1·3.3MeCN·MeOH). To a stirred, colorless solution of $shaH_2$ (0.08 g, 0.50 mmol) in a solvent mixture of MeOH (10 mL) and MeCN (10 mL) was added solid $MnBr_2$ (0.11 g, 0.50 mmol). The resulting yellow-orange suspension was kept under magnetic stirring at room temperature for about 30 min without any noticeable color change. To this solution was slowly added diethylamine (Et_2NH; 103 μL, 1.00 mmol) and the mixture turned dark brown over a period of 1 h. The dark colored solution was filtered, and the resulting filtrate was left to evaporate slowly at room temperature. After 20 days, dark-red plate-like crystals of **1**·3.3MeCN·MeOH had appeared and were collected by filtration, washed with cold MeOH (2 × 2 mL) and Et_2O (2 × 3 mL), and dried in air. The yield was 32% (based on the total available Mn). The air-dried microcrystalline solid was analyzed as lattice solvent-free **1**. Anal. Calcd for $C_{64}H_{60}Mn_9N_{10}O_{28}$: C, 40.21; H, 3.16; N, 7.33%. Found: C, 40.32; H, 3.33; N, 7.24%. Selected IR data (cm^{-1}): 3445 (mb), 2974 (m), 2939 (m), 2875 (m), 2804 (m), 2739 (m), 2679 (m), 1597 (w), 1569 (w), 1514 (w), 1473 (s), 1433 (s), 1397 (s), 1385 (m), 1364 (m), 1330 (w), 1287 (w), 1257 (w), 1170 (vs), 1076 (m), 1035 (vs), 928 (w), 849 (m), 804 (s), 757 (w), 679 (w), 612 (w), 564 (w), 521 (w), 468 (m), 456 (m), 434 (w).

Physical measurements

Elemental analyses (C, H, and N) were performed by the Microanalytical Service of the University of Patras. Infrared (IR) spectra (4000–400 cm^{-1}) were recorded in the solid state using a PerkinElmer 16 PC spectrometer with samples prepared as KBr pellets. Powder-XRD (p-XRD) measurements were carried out using a Rigaku Miniflex 6G X-ray diffractometer. Magnetic susceptibility studies were performed in the temperature range 1.8–300 K using a Quantum Design MPMS XL SQUID magnetometer equipped with a 7 T magnet. The direct current (dc) magnetic susceptibility measurements were performed with an external magnetic field of 1000 Oe in the temperature range of 5–300 K, and the alternating current (ac) measurements were performed in a 3.5 Oe ac field oscillating at different frequencies from 1 to 1500 Hz. The experimental magnetic susceptibility data were corrected for diamagnetism estimated from Pascal's tables and sample holder calibration.[60] Low-temperature (40 mK–2.0 K) magnetization (*M*) *versus* field (*H*) measurements were performed on a single crystal using an array of μ-SQUIDs inside a dilution refrigerator equipped with a 3D vector magnet.[61] The high sensitivity of this magnetometer allows the study of single crystals of SMMs of the order of 10–500 μm. The field can be applied in any direction with a precision better than 0.1° by separately driving three orthogonal coils. Crystals of **1**·3.3MeCN·MeOH were maintained in mother liquor to avoid degradation and were covered in Apiezon grease for protection during transfer to the μ-SQUIDs and thermalization during subsequent cooling.

Computational studies

The electronic structure of the Mn_9 cluster (**1**) was calculated *ab initio* using CASSCF/RASSI-SO/SINGLE/POLY_ANISO type calculations in OpenMolcas version 24.10.[62] To treat the nine paramagnetic metal centres of **1**, we used a fragmentation approach as an approximation to the electronic structure of the cluster compound. This method avoids calculating an intractably large active space and instead calculates the crystal field levels of all Mn centres individually (see below for details). Since the cluster has C_2 symmetry, it is sufficient to treat the central Mn^{II} ion and only half of the Mn^{III} centres using the full *ab initio* method. The active space in the CASSCF calculation comprised the 3d- and 4d-shells of that single Mn ion (4d-shells are included due to the double shell effect[63]). Generally, all the atoms were calculated this way, after which their low-lying states were mixed using POLY_ANISO, which accounts for magnetic coupling (the dipolar and exchange interactions between magnetic centres). Dipolar coupling was calculated using the program, whereas exchange coupling constants were determined using broken-symmetry DFT calculations with Orca 6.0.[64]

Comments on synthesis

Our group has had longstanding interest in exploring the coordination capabilities of salicylhydroxamic acid ($shaH_2$) and its salicylhydroxime ($shiH_3$) derivative as organic chelates for the preparation of homometallic Mn and heterometallic Mn/Ca clusters with exciting structural motifs, interesting magnetic properties and/or bioinorganic relevance to mimicking the structure and function of the active site of Photosystem II.[65–67] Prior to initiating our efforts toward this goal, it was shown that when carboxylate ions were used in conjunction with $shaH_2$ the resulting complexes were mainly composed of a tetranuclear metallic square base linked to a fifth, apical metal site through those bidentate bridging (or other times terminal and bridging) carboxylate ligands. As a result, pentanuclear $M^{n+}/RCO_2^-/shi^{3-}$ complexes have been very stable crystalline products for various metal ions (M^{n+}) and different carboxylate (RCO_2^-) groups.[68] In this work, we removed RCO_2^- ions from the reaction mixture and replaced them with various inorganic anions, such as halides, ClO_4^-, and NO_3^-. We have also accounted for the basicity of carboxylate ions by adding the external base Et_2NH. Therefore, the one-pot reaction of $MnBr_2$, $shaH_2$ and Et_2NH in a 1 : 1 : 2 molar ratio, in a solvent mixture of MeOH/MeCN (1 : 1 v/v), gave a dark brown solution that, upon filtration and slow evaporation at room temperature, afforded dark-red crystals of the $(Et_2NH_2)_2[Mn_9(OH)_4(shi)_8]$ complex (**1**) in 32% yield (based on the total available Mn). The powder XRD spectrum of **1** also confirmed its crystalline nature and phase purity (Fig. S1). Some discrepancies between the experimental and simulated spectra in the low-angle regime are primarily attributed to the loss of lattice solvate molecules (as also confirmed by elemental analyses) and the resulting reduction in crystallinity of the dried sample. The formation of **1** is presented in the balanced equation (eqn (1)) below:

$$9MnBr_2 + 8shiH_3 + 2O_2 + 20Et_2NH \rightarrow (Et_2NH_2)_2\left[Mn_9(OH)_4(shi)_8\right] + 18(Et_2NH_2)Br \quad (1)$$

The reaction that gave **1** is an oxidation, undoubtedly by atmospheric O_2 under the prevailing basic conditions. Analogous reactions with different manganese(II) halides as starting materials all failed to yield single crystals suitable for X-ray diffraction studies. This is most likely due to the ability of Br^- ions to modulate redox reactions and stabilize mixed-valence products of Mn at different oxidation states.[69] Et_2NH has the role of a proton acceptor to facilitate the deprotonation of the $shiH_3$ groups and subsequently the protonation of O^{2-} ions (reduction product of atmospheric O_2) to the resulting, coordinated OH^- groups (*vide infra*). In addition, anionic cluster **1** is stabilized by two $Et_2NH_2^+$ countercations, thus establishing the crucial role of the base in the chemical stabilization and structural elucidation of the reported cluster. Employment of different organic bases, such as NEt_3, Me_2NH, NMe_3, $Bu^n{}_3N$ and Me_4NOH, did not afford crystalline materials but only oily products that we were not able to further characterize. In **1**, the coordinated shi^{3-} groups resulted from the metal ion-assisted transformation of $shaH_2$ under reported synthetic conditions (*vide infra*). Finally, by adjusting the experimental molar ratios of the precursors to the exact stoichiometric equivalents, in an attempt to optimize the isolated

yields, we failed to reproduce the crystals of **1**. It is worth noting that the employed solvent mixture was proved to be a decisive factor for: (i) the growth of suitable crystals of **1** for single-crystal XRD studies (Table S1), (ii) the purity of crystalline product **1**, avoiding contamination from the byproduct $(Et_2NH_2)Br$, which is fairly soluble in MeOH, and (iii) the stabilization of the crystals of **1**, as verified by the role of both MeOH and MeCN as lattice solvate molecules and their participation in intramolecular and intermolecular hydrogen bonding interactions (*vide infra*).

Description of the structure

The crystal structure of **1** consists of $[Mn_9(OH)_4(shi)_8]^{2-}$ anions (Fig. 1) counterbalanced by $Et_2NH_2^+$ cations. In addition, there are MeCN and MeOH solvate molecules in the crystal lattice, which are weakly interacting with the anionic cluster compounds and the countercations (Fig. S2). Selected interatomic distances and angles of **1** are listed in Table S2. The chemical formula of **1** is based on metric parameters, charge-balance considerations, and bond valence sum (BVS)[70] calculations on Mn and selected O atoms (Table S3).

The anionic $[Mn_9(OH)_4(shi)_8]^{2-}$ cluster is built around a C_2-axis, which passes solely through the central Mn^{II} atom (Mn1) and generates two sets of symmetry equivalent Mn^{III} atoms [Mn(1,1′), Mn(2,2′), Mn(3,3′), and Mn(4,4′)]. Mn1 is eight-coordinate in an O_8 set of donor atoms, all arising from the bridging oximate units of shi^{3-} groups (O1, O11, O21, O31, and their symmetry equivalents). The polyhedron that better describes the coordination geometry of Mn1 is that of a close-to-ideal square antiprism (Fig. S3, top), as indicated by the best-fit Continuous Shape Measure (CShM) value of 0.16 (Table S4).[71] CShM values between 0.1 and 3 usually correspond to a non-negligible but still small distortion from ideal geometry. This further agrees with the calculated skew angle, Φ, of 45.1°, which is almost the same with an ideal value of 45°. The distortions from the ideal square antiprismatic geometry can be viewed in terms of: (i) the difference between the d_{pp} (2.442 Å) and d_{in} (2.784 Å) values and (ii) the deviation of the average α angle (the angle between the S_8 axis and the Mn–O vectors) of 58.0° from the ideal value of 54.7° (Fig. S3, bottom).[72] The axial distortion, as calculated by the d_{in}/d_{pp} quotient, is 1.14. The above parameters indicate a compressed square antiprismatic coordination environment for the central Mn^{II} atom in **1**.

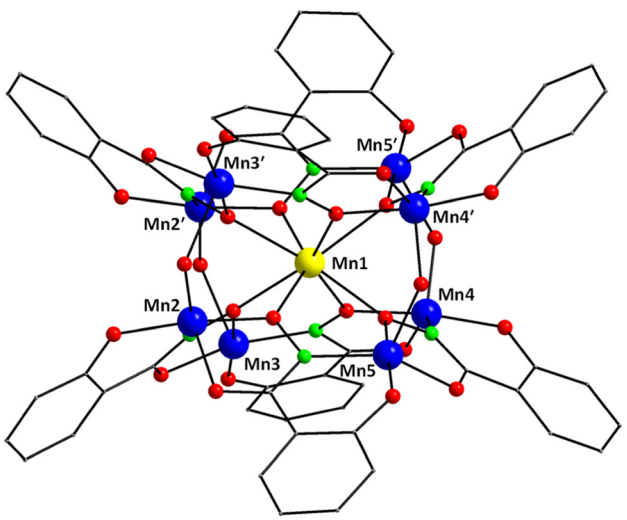

Fig. 1 Partially labeled representation of the anion of complex **1**. H atoms are omitted for clarity. Color scheme: Mn^{II}, yellow; Mn^{III}, blue; O, red; N, green; and C, gray. Symmetry code: (′) 1 – *x*, *y*, 0.5 – *z*.

In contrast, all the surrounding Mn^{III} atoms are five-coordinate with very distorted square pyramidal geometries, as confirmed by analysis of the shape-determining bond angles using the approach of Reedijk and Addison.[73] This yielded values for the trigonality index, τ, of 0.48, 0.20, 0.54, and 0.47 for Mn2, Mn3, Mn4 and Mn5, respectively, where τ is 0 and 1 for perfect square pyramidal and trigonal bipyramidal geometries, respectively. Notably, Trávníček and coworkers have reported the significant uniaxial magnetic anisotropy (D = −2.2 to −3.7 cm^{-1}) of two mononuclear, five-coordinate Mn^{III} complexes bearing tetradentate Schiff base ligands; the results were supported by both experimental data and theoretical calculations,[74] further corroborating the work of Maurice and coworkers on magnetostructural relations for the nonintuitive zero-field splitting in Mn^{III} complexes.[75] These findings point forward promising magnetic properties for compound **1**.

The overall conformation of the nine Mn atoms in **1** can be described in three inter-related ways: (i) as a very distorted capped cube, supported by the smallest derived CShM value of 15.36, with the eight Mn^{III} atoms occupying the corners of the cube and the Mn^{II} atom being the 'capping-inside-the-cube' atom, (ii) as a double-decker $\{Mn^{III}_4–Mn^{II}–Mn^{III}_4\}$ structure with the $\{Mn_4\}$ subunits acting as 'decks' encapsulating the central Mn^{II} atom, and (iii) as two distorted square pyramidal $\{Mn^{III}_4Mn^{II}\}$ subunits sharing a common Mn^{II} apex (Fig. 2, top). Adopting the latter description for simplicity, the two symmetry-related square bases are each composed of four Mn^{III} atoms that are bridged by the oximate (NO^-) groups of four shi^{3-} ligands yielding a regular $\{12\text{-}MC_{Mn(III)N(shi)}\text{-}4\}$ metallacrown subunit. All oximate O atoms are further linked to the apical Mn^{II} atom, resulting in an overall $\eta^1{:}\eta^1{:}\eta^2{:}\eta^1{:}\mu_3$ coordination mode for all shi^{3-} ligands in **1**. Each Mn^{III} atom of the square base is connected to the other $\{Mn_4\}$ 'deck' through the O atom of a $\mu\text{-}OH^-$ group (O41, O41′, O42, and O42′). Thus, complex **1** has an overall $[Mn^{II}Mn^{III}_8(\mu\text{-}OH)_4(\mu_3\text{-}NO)_6]^{16+}$ core (Fig. 2, bottom). Completion of the coordination sphere of each Mn^{III} atom is achieved by the two chelating parts of each shi^{3-} group, namely the $\{C_3O_{phenoxido}N_{oximato}\}$ and $\{CO_{alkoxido}N_{oximato}O_{oximato}\}$ arrays of atoms. The Mn^{III} atoms form a near-planar square, with Mn···Mn separations of 4.598(1)–4.664(1) Å and Mn···Mn···Mn angles spanning the range 84.2–92.7°, deviating only slightly from the ideal 90°. The almost perfectly planar $\{Mn_4\}$ unit is clearly due to the large Mn–N–O–Mn torsion angles of 166.3° (Mn4–N21–O21–Mn5), 165.3° (Mn2–N1–O1–Mn3), 167.6° (Mn3–N11–O11–

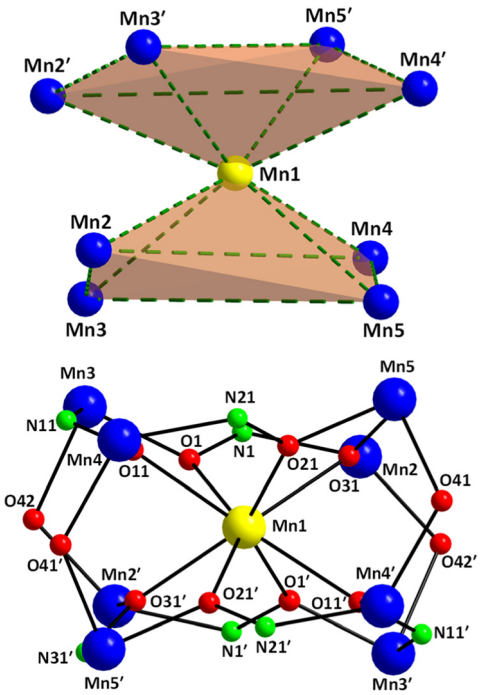

Fig. 2 (Top) The {Mn_9} topology; the dark green dashed lines represent virtual Mn···Mn bonds. (Bottom) Labeled representation of the complete $[Mn_9(\mu\text{-}OH)_4(\mu_3\text{-}NO)_6]^{16+}$ core of **1**. The Mn···Mn distances indicated with dashed lines are Mn1···Mn2 = 3.548(1); Mn1···Mn3 = 3.772(2); Mn1···Mn4 = 3.624(1); Mn1···Mn5 = 3.679(1); Mn2···Mn3 = 4.648(1); Mn2···Mn4 = 6.688(1); Mn2···Mn5 = 4.664(1); Mn3···Mn4 = 4.598(1); Mn3···Mn5 = 6.242(1); and Mn4···Mn5 = 4.625(1). Symmetry code: (′) 1 − *x*, *y*, 0.5 − *z*. The color scheme and symmetry code are the same as those in Fig. 1.

Mn4), and 179.6° (Mn5–N31–O31–Mn2), very close to the ideal linearity of 180°.

The shortest intermolecular Mn···Mn separation is 7.245 Å and includes Mn2 and Mn4 atoms of neighboring clusters. Finally, the space-filling representation (Fig. S4) shows that **1** adopts a nanosized, almost spherical motif with dimensions of ~1.68 and ~1.63 nm, as defined by the longest C···C distances. Although complex **1** joins a large group of enneanuclear Mn clusters, with most of them belonging to the families of [3 × 3] grids, the $\{Mn_9^{II/III/IV}\}$-tripodal cages and the $\{Mn_9^{III}\}$-salicylaldoxime based clusters, there are still several structural and magnetic features that are worthy of being discussed. Therefore, we have collected all of them in Table S5 for a convenient comparison of their formulae, oxidation state descriptions, and pertinent magnetic data such as their ground state spin (*S*) values and – in cases where they are SMMs – their effective energy barriers for magnetization reversal. From the listed compounds, it appears that: (i) complex **1** is structurally unique, (ii) the $\{Mn^{II}Mn_8^{III}\}$ oxidation state description has only been previously reported in three low-spin (*S* = 3/2 or 5/2) and non-SMM compounds, and (iii) compound **1** is the smallest spin SMM with the highest blocking temperature, as confirmed by single-crystal hysteresis studies (*vide infra*).

Magnetic susceptibility studies

Variable-temperature direct-current (dc) magnetic susceptibility measurements were performed on a powdered microcrystalline sample of **1** in a 1 kG (0.1 T) field and in the 5.0–300 K range. The obtained data are shown as a $\chi_M T$ *vs.* *T* plot in Fig. 3. The $\chi_M T$ product steadily decreases from 17.99 cm^3 K mol^{-1} at 300 K to 3.60 cm^3 K mol^{-1} at 5.0 K. The $\chi_M T$ value at 300 K is much less than the spin-only (*g* = 2) value of 28.38 cm^3 K mol^{-1} for one Mn^{II} (d^5; *S* = 5/2) and eight Mn^{III} (d^4; *S* = 2) non-interacting ions, indicating the presence of dominant antiferromagnetic exchange interactions and a small ground state *S* value. In fact, the experimental $\chi_M T$ at 5 K is in good agreement with an *S* = 5/2 spin ground state, for which the expected spin-only (*g* = 2) value is 4.38 cm^3 K mol^{-1}.

To confirm the indicated *S* = 5/2 ground state of complex **1** and to determine the magnitude and sign of *D*, magnetization (*M*) *vs.* dc field measurements were made on restrained samples in the magnetic field (*H*) and temperature ranges of 0.1–5.0 T and 1.8–10.0 K, respectively. Subsequently, the data were also collected in the low field range of 0.1–1.0 T in the same temperature regime. The resulting data are shown in Fig. S5 and Fig. 4 as a reduced magnetization ($M/N\mu_B$) *vs.* H/T plot, where *M* is the magnetization, *N* is Avogadro's number, and μ_B is the Bohr magneton. Both sets of data were fit using the program MAGNET[76] to a model that assumes only that the ground state is populated at these temperatures and magnetic fields, includes isotropic Zeeman interactions and axial zero-field splitting ($D\hat{S}_z^2$), and incorporates a full powder average. The corresponding spin Hamiltonian is given using eqn (2), where $\hat{S}_z$ is the easy-axis spin operator and μ_0 is the vacuum permeability. The last term in eqn (2) is the Zeeman energy associated with an applied magnetic field.

$$\mathcal{H} = D\hat{S}_z^2 + g\mu_B\mu_0\hat{S}\cdot H \quad (2)$$

The best fit is shown as the solid lines in Fig. S5 and Fig. 4 and was obtained with *S* = 5/2, *g* = 1.86(3), and *D* = −1.57(2) cm^{-1} for the 0.1–5.0 T field region, while the fit for the low-fields yielded very good results for *S* = 5/2, *g* = 1.95(2), and *D* =

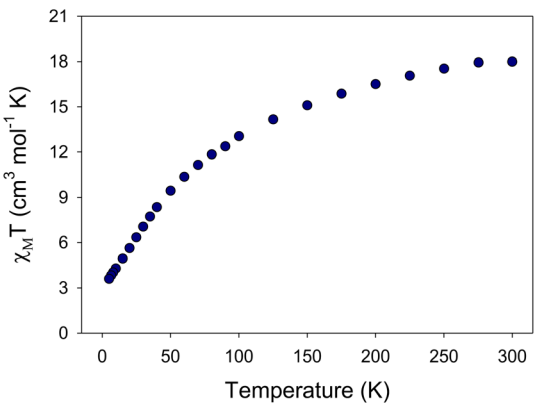

Fig. 3 Temperature dependence of the $\chi_M T$ product for complex **1** at an applied dc field of 1000 Oe.

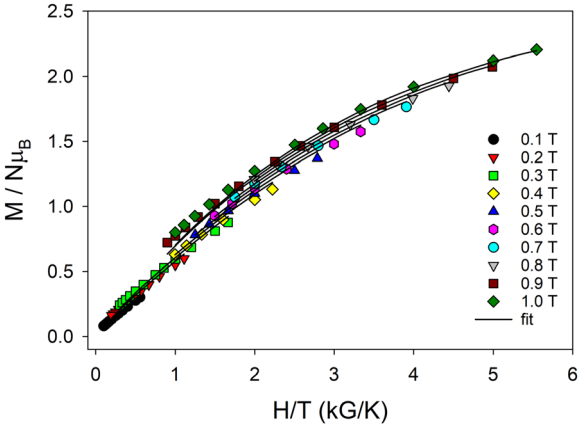

Fig. 4 Magnetization (*M*) *vs.* field (*H*) and temperature (*T*) data, plotted as reduced magnetization ($M/N\mu_B$) *vs.* H/T, for complex **1** at applied fields of 0.1–1.0 T, in the 1.8–10 K temperature range. The solid lines are the fit of the data; see the text for the fit parameters.

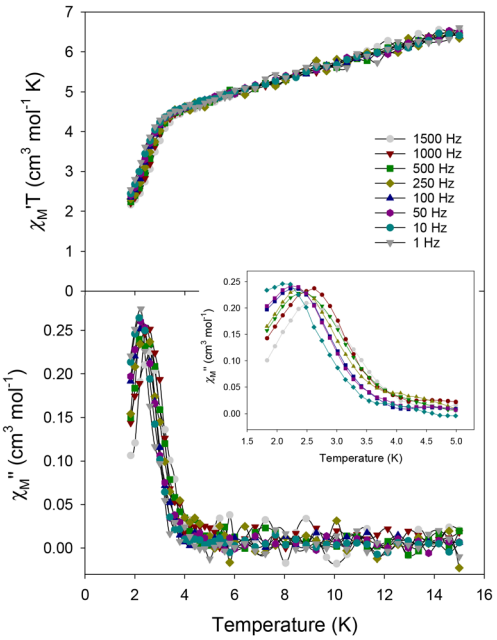

Fig. 5 Plot of the in-phase (χ'_M) (as $\chi'_M T$, top) and out-of-phase (χ''_M, bottom) ac susceptibility signals of complex **1** in a 3.5 G field oscillating at the indicated frequencies. (Inset) A zoomed area of the χ''_M *vs.* *T* plot in the 1.8–5.0 K temperature region. The solid lines are guides only.

$-2.51(2)$ cm^{-1}. In both high- and low-field models, alternative fits with $S = 3/2$ or 7/2 were rejected because they gave unreasonable values of *g*. The deviations of fitted *g* values from the free-electron or ionic expectations are well documented in high-nuclearity 3d-based SMMs when reduced-spin models are employed, particularly when low-lying excited states are not explicitly included in the spin Hamiltonian. The low-field fits are more sensitive to the lowest Kramers doublet only and yield *g* values (≈1.95) much closer to those independently inferred from the ac susceptibility data ($g \approx 1.92$, *vide infra*).

Alternating current (ac) susceptibility studies are a powerful complement to dc studies for determining the spin ground state of a cluster compound because they preclude any complications arising from the presence of a dc field. Thus, ac studies were carried out on **1** in the 1.8–15 K range, using a 3.5 G ac field oscillating at frequencies in the 1–1500 Hz range, as an independent determination of its ground state *S*. For complex **1**, the in-phase $\chi'_M T$ signal below 15 K decreases linearly with decreasing temperature until ~4.5 K, indicating depopulation of low-lying excited states with *S* greater than the ground state, before a further steep decrease at $T < 4$ K (Fig. 5, top). Extrapolation of the plot to 0 K from above 5 K (to avoid the decrease at lower *T* due to the slow relaxation (see below)) gives a value of ~4 cm^3 K mol^{-1}. This agrees with an $S = 5/2$ ground state and $g \sim 1.92$, in very good agreement with the dc magnetization fit. Note that $S = 3/2$ and 7/2 ground states would be expected to give $\chi'_M T$ values of ~2 and ~8 cm^3 K mol^{-1}, respectively, clearly very different from the experimental value. We conclude that complex **1** has an $S = 5/2$ ground state, and this is rationalized in terms of antiferromagnetic interactions between the four Mn^{III} atoms within each 'deck', as promoted by the oximato bridges, yielding two local $S_{Mn_4} = 0$ states and a high-spin Mn^{II} determining the overall spin of the system. Below ~4.5 K, the decrease in the $\chi'_M T$ *vs.* *T* plot is frequency-dependent, and there is a concomitant appearance of frequency-dependent out-of-phase χ''_M signals (Fig. 5, bottom), whose peak maxima are visible above 1.8 K, the operating minimum temperature of the SQUID magnetometer. Such behavior is indicative (but not diagnostic) of the superparamagnetic-like properties of an SMM.

Magnetization *vs.* dc field hysteresis loops

Confirmation of the SMM behavior was sought by magnetization *vs.* dc field scans on single crystals of **1** that had been kept in contact with mother liquor using an array of micro-SQUIDs.[77] Magnetization hysteresis loops were observed below ~2.0 K, at which point the coercivity increases with decreasing temperature (Fig. 6 and S6, top) and increasing field sweep rate (Fig. 6 and S6, bottom), as expected for an SMM below its blocking temperature (T_B). In the vast majority of 3d-cluster based SMMs, the first step in sweeping the field from one saturating value to the other occurs in zero field where the potential energy double-well is symmetric and M_s levels on one side of the barrier are degenerate (in resonance) with those on the other side, allowing tunneling to occur through the anisotropy barrier. The exception, as seen in **1**, is when the first step is slightly shifted away from the zero field by the exchange-bias effect, the weak interaction of an SMM with a neighboring SMM.[78] The steps are thus positions of increased magnetization relaxation rate. Furthermore, the hysteresis loops do not show resolved steps characteristic of quantum tunneling of magnetization (QTM), but this is not surprising, as high-nuclearity SMMs are more susceptible to distributions of their molecular environments, which reflect in various step-broadening effects resulting from low-lying excited states or

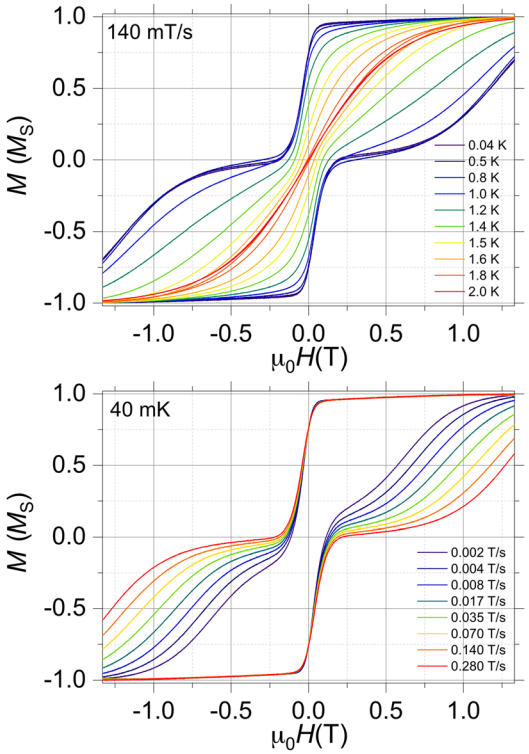

Fig. 6 Magnetization (*M*) *vs.* field (*H*) hysteresis loops for a single crystal of complex **1** at the indicated temperatures (top) and field sweep rates (bottom). The magnetization is normalized to its saturation value (M_s).

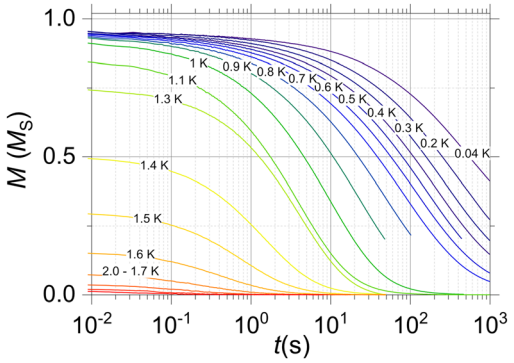

Fig. 7 Magnetization (*M*) *vs.* time (*t*) decay plots in zero dc field for a single crystal of **1**. The magnetization is normalized to its saturation value, M_S.

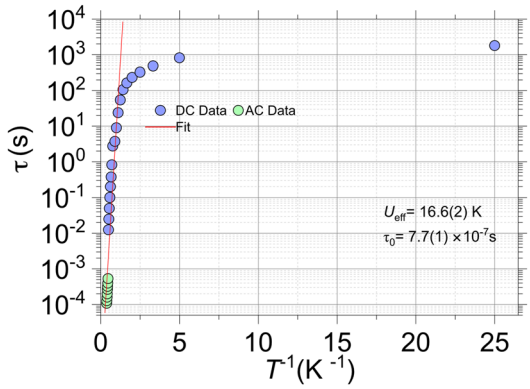

Fig. 8 Arrhenius plot of the relaxation time (τ) *vs.* $1/T$ for **1** using data obtained from ac susceptibility and the dc magnetization decay measurements of Fig. 7. The solid line is the fit of data in the thermally activated region to the Arrhenius equation; see the text for the fit parameters.

disordered ligands and solvent molecules of crystallization in the vacancies between cluster compounds.

In such cases, the presence of QTM is best confirmed by other methods, such as the detection of a temperature-independent relaxation rate at very low temperatures through magnetization decay with time studies. To this end, the magnetization of the sample was first saturated in one direction with a large applied field at ~5 K, the temperature was decreased to a chosen value in the 0.04–2.0 K range, the applied field was removed, and the magnetization of the sample was monitored with time. The resulting data are shown in Fig. 7. The decay data at each temperature were analyzed to give a set of relaxation time (τ) *vs.* temperature data, which were used, in conjunction with the relaxation times derived from the ac measurements, to construct the combined Arrhenius plot of Fig. 8 based on the Arrhenius relationship of eqn (3), where τ_0 is the pre-exponential factor, U_{eff} is the mean effective barrier to relaxation, and k is the Boltzmann constant.

$$\tau = \tau_0 \exp(U_{\text{eff}}/kT) \quad (3a)$$

$$\ln \tau = \ln \tau_0 + U_{\text{eff}}/kT \quad (3b)$$

The fit of the thermally activated region is shown as the solid line in Fig. 8 and gives for **1** the parameters: U_{eff} = 16.6(2) K (11.5(2) cm^{-1}) and $\tau_0 = 7.7(1) \times 10^{-7}$ s. At the lowest temperatures (below ~0.1 K), the relaxation time becomes temperature-independent, as expected for the relaxation only occurring *via* the ground state M_S levels. This temperature independence of relaxation is a characteristic signature of QTM through the anisotropy barrier. Considering the experimental D value of −2.51 cm^{-1}, obtained from the fit of the magnetization *vs.* low-field data, the calculated maximum U barrier for an SMM with S = 5/2 is $U = (S^2-1/4)|D|$ = ~15 cm^{-1}, which is in very good agreement with the experimental U_{eff}, suggesting that thermally-assisted magnetization relaxation occurs *via* the higher energy M_S states of the S = 5/2 manifold.

Theoretical analysis

To rationalize the origin of the unusually strong axial magnetic anisotropy of **1** responsible for its SMM behavior, *ab initio* calculations at the CASSCF/SO-RASSI level of a mononuclear Mn (II) fragment have been performed. Table S7 shows the energies of the three Kramers doublets (KD) resulting from the zero-field splitting (ZFS) of the ground S = 5/2 term of the Mn(II) ion. We can see that the overall splitting is *ca.* 0.05 cm^{-1}, which is explained by a very large energy of the first excited term (*ca.* 30 000 cm^{-1}, Table S7), exceeding the spin–orbit

coupling of the Mn(II) ion by several orders of magnitude (Table S7). For the same reason, the *g*-tensor of the ground S = 5/2 term of Mn(II) practically coincides with the free electron one (Table S12). The ZFS splitting of Mn(II) is two orders of magnitude smaller than the one inferred from the fitting of the low-temperature magnetic data of **1** (Fig. 4 and 8). This means that the intrinsic ZFS splitting of the ground term of the Mn(II) ion cannot be the reason for the observed magnetization blocking.[79–81] Hence, this must be due to the interaction with the surrounding Mn(III) ions, despite the fact that their magnetism apparently does not show up at low temperature.

Similar *ab initio* analysis has been performed for the four inequivalent Mn(III) centres. Tables S8–S11 show that the ZFS of the ground S = 2 term of these ions is *ca.* 12 cm^{-1}, *i.e.* they exhibit much stronger ionic anisotropy than the Mn(II) ion. This may be explained by the smaller energy gap to the excited states ($\geqslant$12 000 cm^{-1}) and a larger spin–orbit coupling constant of Mn(III) leading to partial unquenching of the orbital momentum. The five levels originating from the S = 2 ground term are fully split according to the lack of local symmetry on the Mn(III) centres. Nevertheless, the levels still pair into doublets showing relatively small tunneling gaps. Furthermore, the value of the main *g*-factor of the ground doublet is close to 8 (Table S12), corresponding to spin projections, M = ±2, which points to relatively strong axiality of the ground doublet. This is in line with an earlier observation of strong axiality of magnetic ions with high $J(S)$ in non-symmetric environments.[82] Since the S = 2, M = S state is well approximated by a single Slater determinant, the ionic anisotropy of Mn(III) centres can also be described using DFT. Table S14 shows that the obtained DFT values of ionic anisotropy parameters for Mn2 are close to those of the CASSCF.

The calculated anisotropy axes of the Mn(III) ions in **1** are oriented along the elongated Mn–O bonds of the square pyramidal apex, as shown in Fig. 9. Mn3 has a coordination environment closest to a true square pyramid, which manifests as near-perfect alignment of its anisotropy axis along the apical Mn–O bond. The orientation of the anisotropy axes along the square pyramidal apex and the bent local structure at the oxygen atoms leads to a low angle between the axes of the surrounding Mn(III) and the central Mn(II) (Table S15). All axes lie approximately perpendicular to the surface of the two Mn_4 deckers, whereas their symmetric alignment around the axis perpendicular to the deckers underlies the high axiality of the low-lying exchange doublets, ultimately explaining the SMM behavior of **1** (*vide infra*).

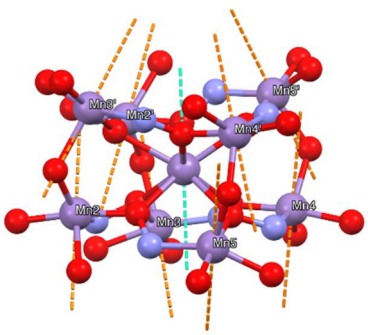

Fig. 9 Anisotropy axes of Mn2–Mn5 (orange) and Mn1 (cyan). The numeration of manganese atoms is the same as that in Fig. 2.

The magnetic interaction between the manganese ions contains two contributions, the exchange and the magnetic dipolar interaction. The exchange parameters have been extracted from conventional broken-symmetry (BS) DFT calculations of **1** in its experimental geometry (see the SI). The obtained exchange coupling constants between manganese ions, reported to S = 5/2 for Mn(II) and S = 2 for Mn(III), are listed in Table S13 (positive values correspond to ferromagnetic coupling). It is clear that the overall interaction between Mn(III) ions is antiferromagnetic, as expected. Some coupling constants have large values, notably for Mn4–Mn5* and Mn4*–Mn5 pairs, which explains why $\chi_M T$ for **1** is far from the sum of susceptibilities of individual manganese ions at room temperature (Fig. 3). The magnetic dipolar interaction between manganese ions has been calculated with the Poly_Aniso module of OpenMolcas using the ionic anisotropy data for mononuclear fragments obtained in the previous CASSCF calculations.[83] Their effect on the exchange spectrum of **1** is by two orders of magnitude smaller than from the exchange interaction (Table 1). This is in contrast to polynuclear lanthanide complexes where exchange and magnetic dipolar coupling give comparable contributions to the magnetic interaction between Ln ions, which is explained by a stronger exchange interaction and smaller local magnetic moments in transition metal compounds.[84]

A direct simulation of magnetic susceptibility of **1** does not seem feasible because of the many exchange states involved in the $\{Mn^{II}Mn^{III}_8\}$ cluster (>2 million states). Therefore, to gain further insight, we calculated the magnetism of a smaller fragment $\{Mn^{II}Mn^{III}_4\}$ involving only the non-equivalent Mn(III) ions, *i.e.*, Mn(2–5). The magnetic susceptibility was simulated

Table 1 Energies of low-lying exchange KDs (cm^{-1}) of a $\{Mn^{II}Mn^{III}_4\}$ fragment calculated in different approximations

Dipolar + ZFS on all Mn sites	Exchange + ZFS on all Mn sites	Dipolar + exchange + ZFS on all Mn sites (complete model)	Dipolar + exchange (all Mn(III) isotropic)
0.000	0.00	0.00	0.000
0.027	2.15	2.12	0.025
0.081	4.42	4.37	0.038
0.206	6.84	6.75	2.16
0.262	9.44	9.34	2.18
0.312	10.49	10.70	2.19
0.521	11.96	12.19	2.19
0.581	12.35	12.30	5.33
0.606	12.78	12.88	5.34
0.638	12.97	13.14	5.35
0.681	13.60	13.80	5.36
0.717	14.23	14.25	5.37
0.776	14.46	14.60	6.42
0.806	15.07	15.11	6.44

approximately by doubling the susceptibility of the fragment $\{Mn^{II}Mn^{III}_4\}$ and then extracting the susceptibility of a single Mn(II) center. The result in Fig. S10 shows that the calculated $\chi_M T$ reaches saturation faster than the experimental one because in our model the exchange interaction between Mn(III) ions from the two equivalent groups was neglected, which strongly reduced the spread of the exchange levels. The energies of calculated low-lying exchange levels using *ab initio* magnetic coupling and ionic anisotropic parameters are given in Table 1.

We can see that the lowest three levels in Table 1 are visibly separated from the excited ones pointing to their Mn(II) origin. This is in line with the single-Mn(II) based model used for the simulation of magnetization of **1** (Fig. 4) which yielded a *g*-factor value close to 2.0, typical of the Mn(II) in coordination complexes. Our calculations give close *g*-factor values of 1.95, 1.97, and 2.34. According to the results presented in Table 1, the main reason for the splitting of the three Kramers doublets is the concomitant presence of the exchange interaction between manganese ions and the ZFS splitting on the Mn(III) ions, while other factors (intrinsic ZFS at Mn(II) and the magnetic dipolar interaction) play a minor role.

Thus, we conclude that the low-temperature magnetism of **1** is effectively provided by the Mn(II) ion alone, whose ionic anisotropy is induced by strong ZFS at Mn(III) ions through their exchange interaction with the Mn(II) ion. According to Table 1, the obtained ZFS at Mn(II) is rather equidistant, while the axial anisotropic contribution in eqn (2) alone gives for the energies of the three KDs: $-(25/4)|D|$, $-(9/4)|D|$ and $-(1/4)|D|$. In order to make these levels equidistant, the rhombic anisotropic contribution $E(\hat{S}_x^2 - \hat{S}_y^2)$ should involve E of comparable order of magnitude with D, which will lead to a strong admixture of the two excited KDs, $M = \pm 3/2, \pm 1/2$, to the ground KD, $M = \pm 5/2$. As a result, the ground KD will not be sufficiently axial and will be subject to intense QTM precluding the magnetization blocking in **1**. This is in contradiction with the SMM behavior of the complex and is not supported by our *ab initio* calculations either, which show in contrast that both transversal *g*-factors of the ground KD are $g_{x,y} = 0.00001$ pointing to the high axiality of the latter. The main *g*-factor, $g_z = 10.9$, supports the $M = \pm 5/2$ origin of the ground KD and corresponds to the main magnetic axis perpendicular to the C_2 axis of the complex (Fig. 10). Given this high axiality, underlined by the symmetric arrangement of the anisotropy axes on the Mn(III) ions (see Fig. 9), the ZFS of Mn(II) can be simulated by adding a fourth-order axial anisotropy term, $D'\hat{S}_z^4$, allowing for $S = 5/2$, to the already considered second-order one. To achieve equidistance, the parameter D' should be positive and amount to $(2/29)|D|$. The inferred high axiality of the ZFS on Mn(II) supports earlier findings of highly axial low-lying doublets in non-symmetric complexes combining isotropic and axial magnetic ions.[85,86] Finally, we note that the contribution to the ZFS on Mn(II) from the surrounding Mn(III) ions can be considered in a good approximation additive. Then accounting for the neglected manganese ions in the calculations of Table 1 will merely double the ZFS splitting between the three KDs. Then the overall splitting of $S = 5/2$ on Mn(II) will achieve *ca.* 9 cm^{-1}, which agrees well with the fitted value for the height of the blocking barrier extracted from the dc and ac magnetic susceptibility (Fig. 8).

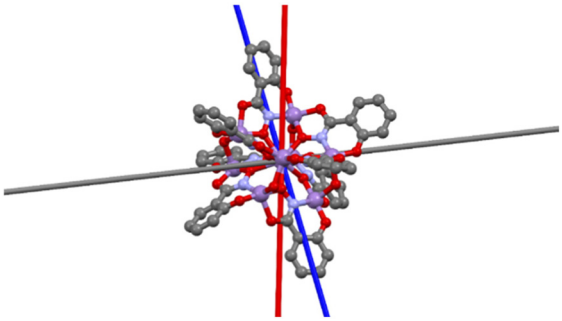

Fig. 10 Calculated main magnetic axes corresponding to the lowest three KDs in **1**, effective $S = 5/2$ (blue), and its ground KD (red). The symmetry C_2 axis is shown in grey. Purple spheres are manganese ions.

Conclusions

In summary, we have reported the synthesis of a mixed-valence $(Et_2NH_2)_2[Mn^{II}Mn^{III}_8(OH)_4(shi)_8]$ (**1**) cluster assembled exclusively from salicylhydroximate groups, which facilitate the formation of a striking double-decker architecture. The structure features a central eight-coordinate Mn^{II} ion encapsulated by a magnetically coupled ring of eight five-coordinate Mn^{III} centers with distorted coordination geometries. Detailed magnetic investigations reveal an $S = 5/2$ ground state combined with a remarkably large axial anisotropy ($D = -2.5$ cm^{-1}), an uncommon feature for a system containing a formally isotropic Mn^{II} center. The synergy between the spin ground state and molecular anisotropy endows complex **1** with clear single-molecule magnet (SMM) behavior, manifested by entirely visible out-of-phase signals and open magnetic hysteresis loops, which give rise to an effective barrier of 16.6 K for magnetization reversal.

Computational analysis has elucidated the origin of the unexpectedly strong magnetic anisotropy of the central Mn^{II} ion in **1** as arising from the interplay between the axial magnetic anisotropy of the surrounding Mn^{III} ions and the relatively strong exchange interaction between them. The situation in which a typical isotropic magnetic ion is solely responsible for the anisotropic magnetism and the magnetization blocking of the entire polynuclear complex has not yet been reported, to the best of our knowledge. The necessary conditions for this are a large number of magnetic neighbors of the isotropic ion exhibiting strong axial magnetic anisotropy and a relatively strong antiferromagnetic exchange interaction between them. All these conditions are perfectly met in the reported $\{Mn_9\}$ cluster, which thus allowed us to demonstrate this unusual SMM behavior.

Beyond its structural elegance, this $\{Mn_9\}$ system establishes a rare magnetic paradigm in which anisotropy is effec-

tively imposed on an isotropic center through cooperative exchange coupling, offering new design principles for engineering unconventional SMMs.

Experiment

A dark-red single-crystal of complex **1**·3.3MeCN·MeOH (0.13 × 0.20 × 0.26 mm) was taken directly from the mother liquor and immediately cooled to 160(2) K. X-ray diffraction data were collected on a Rigaku R-AXIS SPIDER Image Plate diffractometer using graphite-monochromated CuKα (λ = 1.54178 Å) radiation. Data collection (ω-scans) and processing (cell refinement, data reduction, and empirical absorption correction) were performed using the CrystalClear program package.[87] The structure of **1** was solved by direct methods using SHELXS ver. 2013/1,[88] and refined by full-matrix least-squares techniques on F^2 with SHELXL ver. 2014/6.[89a] All H atoms were introduced at calculated positions and refined as riding on their respective bonded atoms. All non-H atoms were refined anisotropically. The presence of additional solvent molecules that could not be modelled, even with restraints, was detected by the residual peaks located in certain areas of the unit cell. Consequently, SQUEEZE (from PLATON)[89b] was used to calculate the void space (460 Å^3) and the electron count (115 e, which accounts for 5.23 MeCN per unit cell), as well as extract a new HKL file. All parameters reported in the CIF account for the total solvent molecule content.

The estimated number of MeCN solvent molecules located at the Wyckoff 4b positions (0, 1/2, 0) is 5.23 per cell or 1.3 per formula unit and they are distributed within channels formed in the structure of **1**. The lattice solvents, as well as the countercations, are located within channels formed between clusters along the [1 −1 0] and [1 1 0] crystallographic directions. Various figures of the structure were created using Diamond 3 and Mercury software packages.[90] The unit cell parameters, structure solution, and refinement details of **1** are summarized in Table S1. Further crystallographic details of compound **1** can be found in the corresponding CIF file provided in the SI.

Author contributions

All authors gave approval to the final version of the manuscript. K. H. B. and E. S. K. contributed to the complete synthesis and spectroscopic characterization of the reported compound. C. P. R. and V. P. acquired the crystallographic (single-crystal and p-XRD) data and provided the supramolecular description of the coordination compound, while A. M. M. and G. C. collected and evaluated the bulk magnetic data of complex **1**. W. W. and E. M. P. carried out the single-crystal magnetic hysteresis measurements, while M. K., V. V. and L. F. C. performed the computational studies of **1**. Th. C. S. conceived the research idea and wrote the paper, with contributions from all co-authors.

Conflicts of interest

There are no conflicts to declare.

Data availability

Supplementary information (SI): experimental, crystallographic, structural and spectroscopic data, supramolecular figures, magnetism (bulk and single-crystal) plots, and data from the theoretical calculations performed on complex **1** that support the findings of this study. See DOI: **https://doi.org/10.1039/d6qi01087c**.

CCDC 2535214 (**1**) contains the supplementary crystallographic data for this paper.[91]

Acknowledgements

W. W. thanks the German Research Foundation (DFG) for the Gottfried Wilhelm Leibniz Award, ZVN-2020_WE 4458-5. E. M.-P. thanks the Alexander von Humboldt Fellowship for Experienced Researchers for support. G. C. thanks the US National Science Foundation for support (CHE-1900321) and the University of Florida.

References

1 C. Papatriantafyllopoulou, E. E. Moushi, G. Christou and A. J. Tasiopoulos, Filling the gap between the quantum and classical worlds of nanoscale magnetism: giant molecular aggregates based on paramagnetic 3d metal ions, *Chem. Soc. Rev.*, 2016, **45**, 1597–1628.
2 D. Gatteschi, R. Sessoli and J. Villain, *Molecular Nanomagnets*, Oxford University Press, Oxford, 2006.
3 L. Bogani and W. Wernsdorfer, Molecular spintronics using single-molecule magnets, *Nat. Mater.*, 2008, **7**, 179–186.
4 E. Moreno-Pineda and W. Wernsdorfer, Measuring molecular magnets for quantum technologies, *Nat. Rev. Phys.*, 2021, **3**, 645–659.
5 W. Wernsdorfer and M. Ruben, Synthetic Hilbert Space Engineering of Molecular Qu*d*its: Isotopologue Chemistry, *Adv. Mater.*, 2019, **31**, 1806687.
6 E. Coronado, Molecular magnetism: from chemical design to spin control in molecules, materials and devices, *Nat. Rev. Mater.*, 2020, **5**, 87–104.
7 (*a*) E. Coronado and P. Day, Magnetic molecular conductors, *Chem. Rev.*, 2004, **104**, 5419–5448; (*b*) E. Coronado, J. R. Galán-Mascarós, C. J. Gómez-García and V. Laukhin, Coexistence of ferromagnetism and metallic conductivity in a molecule-based layered compound, *Nature*, 2000, **408**, 447–449.
8 L. Spree, F. Liu, V. Neu, M. Rosenkranz, G. Velkos, Y. Wang, S. Schiemenz, J. Dreiser, P. Gargiani, M. Valvidares, C.-H. Chen, B. Büchner, S. M. Avdoshenko and A. A. Popov,

Robust Single Molecule Magnet Monolayers on Graphene and Graphite with Magnetic Hysteresis up to 28 K, *Adv. Funct. Mater.*, 2021, **31**, 2105516.

9 C. Cervetti, A. Rettori, M. G. Pini, A. Cornia, A. Repollés, F. Luis, M. Dressel, S. Rauschenbach, K. Kern, M. Burghard and L. Bogani, The classical and quantum dynamics of molecular spins on graphene, *Nat. Mater.*, 2016, **15**, 164–168.

10 I. V. Krainov, J. Klier, A. P. Dmitriev, S. Klyatskaya, M. Ruben, W. Wernsdorfer and I. V. Gornyi, Giant Magnetoresistance in Carbon Nanotubes with Single-Molecule Magnets $TbPc_2$, *ACS Nano*, 2017, **11**, 6868–6880.

11 A. Cornia, A. C. Fabretti, M. Pacchioni, L. Zobbi, D. Bonacchi, A. Caneschi, D. Gatteschi, R. Biagi, U. Del Pennino, V. De Renzi, L. Gurevich and H. S. J. Van der Zant, Direct Observation of Single-Molecule Magnets Organized on Gold Surfaces, *Angew. Chem., Int. Ed.*, 2003, **42**, 1645–1648.

12 D. Maniaki, E. Pilichos and S. P. Perlepes, Coordination Clusters of 3d-Metals That Behave as Single-Molecule Magnets (SMMs): Synthetic Routes and Strategies, *Front. Chem.*, 2018, **6**, 28.

13 F.-S. Guo, B. M. Day, Y.-C. Chen, M.-L. Tong, A. Mansikkamäki and R. A. Layfield, Magnetic hysteresis up to 80 Kelvin in a Dysprosium metallocene single-molecule magnet, *Science*, 2018, **362**, 1400–1403.

14 J. D. Rinehart and J. R. Long, Exploiting Single-Ion Anisotropy in the Design of f-Element Single-Molecule Magnets, *Chem. Sci.*, 2011, **2**, 2078–2085.

15 Y.-S. Meng, S.-D. Jiang, B.-W. Wang and S. Gao, Understanding the Magnetic Anisotropy toward Single-Ion Magnets, *Acc. Chem. Res.*, 2016, **49**, 2381–2389.

16 A. Vinslava, A. J. Tasiopoulos, W. Wernsdorfer, K. A. Abboud and G. Christou, Molecules at the Quantum–Classical Nanoparticle Interface: Giant Mn70 Single-Molecule Magnets of ~4 nm Diameter, *Inorg. Chem.*, 2016, **55**, 3419–3430.

17 A. J. Tasiopoulos, A. Vinslava, W. Wernsdorfer, K. A. Abboud and G. Christou, Giant Single-Molecule Magnets: A Mn_{84} Torus and its Supramolecular Nanotubes, *Angew. Chem., Int. Ed.*, 2004, **43**, 2117–2121.

18 A. J. Tasiopoulos and S. P. Perlepes, Diol-type ligands as central 'players' in the chemistry of high-spin molecules and single-molecule magnets, *Dalton Trans.*, 2008, 5537–5559.

19 E. K. Brechin, Using tripodal alcohols to build high-spin molecules and single-molecule magnets, *Chem. Commun.*, 2005, 5141–5153.

20 C. J. Milios, Th. C. Stamatatos and S. P. Perlepes, The coordination chemistry of pyridyl oximes, *Polyhedron*, 2006, **25**, 134–194.

21 C. J. Milios, S. Piligkos and E. K. Brechin, Ground state spin-switching via targeted structural distortion: Twisted single-molecule magnets from derivatised salicylaldoximes, *Dalton Trans.*, 2008, 1809–1817.

22 Th. C. Stamatatos, D. Foguet-Albiol, S.-C. Lee, C. C. Stoumpos, C. P. Raptopoulou, A. Terzis, W. Wernsdorfer, S. O. Hill, S. P. Perlepes and G. Christou, Switching On' the properties of single-molecule magnetism in triangular Manganese(III) complexes, *J. Am. Chem. Soc.*, 2007, **129**, 9484–9499.

23 T. N. Nguyen, W. Wernsdorfer, K. A. Abboud and G. Christou, A supramolecular aggregate of four exchange-biased single-molecule magnets, *J. Am. Chem. Soc.*, 2011, **133**, 20688–20691.

24 P. Happ, C. Plenk and E. Rentschler, 12-MC-4 metallacrowns as versatile tools for SMM research, *Coord. Chem. Rev.*, 2015, **289–290**, 238–260.

25 V. L. Pecoraro, A. J. Stemmler, B. R. Gibney, J. J. Bodwin, H. Wang, J. W. Kampf and A. Barwinski, Metallacrowns: A New Class of Molecular Recognition Agents, *Prog. Inorg. Chem.*, 1997, **45**, 83–177.

26 A. M. Ako, I. J. Hewitt, V. Mereacre, R. Clérac, W. Wernsdorfer, C. E. Anson and A. K. Powell, A Ferromagnetically Coupled Mn_{19} Aggregate with a Record S=83/2 Ground Spin State, *Angew. Chem., Int. Ed.*, 2006, **45**, 4926–4929.

27 Th. C. Stamatatos, K. A. Abboud, W. Wernsdorfer and G. Christou, Spin Tweaking' of a High Spin Molecule: A New Mn_{25} Single-Molecule Magnet with an S = 61/2 Ground State, *Angew. Chem., Int. Ed.*, 2007, **46**, 884–888.

28 E. E. Moushi, Th. C. Stamatatos, W. Wernsdorfer, V. Nastopoulos, G. Christou and A. J. Tasiopoulos, A Mn_{17} Octahedron with a Giant Ground-State Spin: Occurrence in Discrete Form and as Multidimensional Coordination Polymers, *Inorg. Chem.*, 2009, **48**, 5049–5051.

29 M. Murugesu, M. Habrych, W. Wernsdorfer, K. A. Abboud and G. Christou, Single-Molecule Magnets: A Mn_{25} Complex with a Record S = 51/2 Spin for an Isolated Molecule, *J. Am. Chem. Soc.*, 2004, **126**, 4766–4767.

30 C. J. Milios, R. Inglis, R. Bagai, W. Wernsdorfer, A. Collins, S. Moggach, S. Parsons, S. P. Perlepes, G. Christou and E. K. Brechin, Enhancing SMM properties in a family of $[Mn_6]$ clusters, *Chem. Commun.*, 2007, 3476–3478.

31 C. J. Milios, R. Inglis, A. Vinslava, R. Bagai, W. Wernsdorfer, S. Parsons, S. P. Perlepes, G. Christou and E. K. Brechin, Toward a Magnetostructural Correlation for a Family of Mn_6 SMMs, *J. Am. Chem. Soc.*, 2007, **129**, 12505–12511.

32 D. Gatteschi and R. Sessoli, Quantum Tunneling of Magnetization and Related Phenomena in Molecular Materials, *Angew. Chem., Int. Ed.*, 2003, **42**, 268–297.

33 W. Wernsdorfer and R. Sessoli, Quantum Phase Interference and Parity Effects in Magnetic Molecular Clusters, *Science*, 1999, **284**, 133–135.

34 S. Hill, R. S. Edwards, N. Aliaga-Alcalde and G. Christou, Quantum Coherence in an Exchange-Coupled Dimer of Single-Molecule Magnets, *Science*, 2003, **302**, 1015–1018.

35 G. A. Craig and M. Murrie, 3d-single ion magnets, *Chem. Soc. Rev.*, 2015, **44**, 2135–2147.

36 J. M. Frost, K. L. M. Harriman and M. Murugesu, The rise of 3-d single-ion magnets in molecular magnetism: towards materials from molecules?, *Chem. Sci.*, 2016, **7**, 2470–2491.

37 M. Feng and M.-L. Tong, Single ion magnets from 3d to 5f: Developments and strategies, *Chem. – Eur. J.*, 2018, **24**, 7574–7594.

38 K. L. M. Harriman, D. Errulat and M. Murugesu, Magnetic axiality: Design principles from molecules to materials, *Trends Chem.*, 2019, **1**, 425–439.

39 O. Waldmann, A criterion for the anisotropy barrier in single-molecule magnets, *Inorg. Chem.*, 2007, **46**, 10035–10037.

40 Th. C. Stamatatos, K. A. Abboud, W. Wernsdorfer and G. Christou, High-Nuclearity, High-Symmetry, High-Spin Molecules: A Mixed-Valence Mn_{10} Cage Possessing Rare T symmetry and an $S = 22$ Ground State, *Angew. Chem., Int. Ed.*, 2006, **45**, 4134–4137.

41 M. Manoli, S. Alexandrou, L. Pham, G. Lorusso, W. Wernsdorfer, M. Evangelisti, G. Christou and A. J. Tasiopoulos, Magnetic "Molecular Oligomers" Based on Decametallic Supertetrahedra: A Giant Mn_{49} Cuboctahedron and its $Mn_{25}Na_4$ Fragment, *Angew. Chem., Int. Ed.*, 2016, **55**, 679–684.

42 C. J. Milios, A. Vinslava, W. Wernsdorfer, A. Prescimone, P. A. Wood, S. Parsons, S. P. Perlepes, G. Christou and E. K. Brechin, Spin Switching via Targeted Structural Distortion, *J. Am. Chem. Soc.*, 2007, **129**, 6547–6561.

43 R. Inglis, S. M. Taylor, L. F. Jones, G. S. Papaefstathiou, S. P. Perlepes, S. Datta, S. Hill, W. Wernsdorfer and E. K. Brechin, Twisting, bending, stretching: strategies for making ferromagnetic [$MnIII_3$] triangles, *Dalton Trans.*, 2009, 9157–9168.

44 N. E. Chakov, S.-C. Lee, A. G. Harter, P. L. Kuhns, A. P. Reyes, S. O. Hill, N. S. Dalal, W. Wernsdorfer, K. A. Abboud and G. Christou, The Properties of the $[Mn_{12}O_{12}(O_2CR)_{16}(H_2O)_4]$ Single-Molecule Magnets in Truly Axial Symmetry: $[Mn_{12}O_{12}(O_2CCH_2Br)_{16}(H_2O)_4]\cdot 4CH_2Cl_2$, *J. Am. Chem. Soc.*, 2006, **128**, 6975–6989.

45 C. J. Milios, A. Vinslava, P. A. Wood, S. Parsons, W. Wernsdorfer, G. Christou, S. P. Perlepes and E. K. Brechin, A Single-Molecule Magnet with a "Twist", *J. Am. Chem. Soc.*, 2007, **129**, 8–9.

46 C. J. Milios, A. Vinslava, W. Wernsdorfer, S. Moggach, S. Parsons, S. P. Perlepes, G. Christou and E. K. Brechin, A Record Anisotropy Barrier for a Single-Molecule Magnet, *J. Am. Chem. Soc.*, 2007, **129**, 2754–2755.

47 R. Bagai and G. Christou, The Drosophila of single-molecule magnetism: $[Mn_{12}O_{12}(O_2CR)_{16}(H_2O)_4]$, *Chem. Soc. Rev.*, 2009, **38**, 1011–1026.

48 C. J. Milios, R. Inglis, A. Vinslava, R. Bagai, W. Wernsdorfer, S. Parsons, S. P. Perlepes, G. Christou and E. K. Brechin, Toward a Magnetostructural Correlation for a Family of Mn_6 SMMs, *J. Am. Chem. Soc.*, 2007, **129**, 12505–12511.

49 P. Abbasi, K. Quinn, D. I. Alexandropoulos, M. Damjanović, W. Wernsdorfer, A. Escuer, J. Mayans, M. Pilkington and Th. C. Stamatatos, Transition Metal Single-Molecule Magnets: A $\{Mn_{31}\}$ Nanosized Cluster with a Large Energy Barrier of ~ 60 K and Magnetic Hysteresis at ~ 5 K, *J. Am. Chem. Soc.*, 2017, **139**, 15644–15647.

50 T. G. Ashebr, H. Li, X. Ying, X.-L. Li, C. Zhao, S. Liu and J. Tang, Emerging Trends on Designing High-Performance Dysprosium(III) Single-Molecule Magnets, *ACS Mater. Lett.*, 2022, **4**, 307–319.

51 Z. Zhu and J. Tang, Lanthanide Single-Molecule Magnets with High Anisotropy Barrier: Where to from Here?, *Natl. Sci. Rev.*, 2022, **9**, nwac194.

52 A. Zabala-Lekuona, J. M. Seco and E. Colacio, Single-Molecule Magnets: From Mn_{12}-Ac to Dysprosium Metallocenes, a Travel in Time, *Coord. Chem. Rev.*, 2021, **441**, 213984.

53 Z. Zhu, C. Zhao, T. Feng, X. Liu, X. Ying, X.-L. Li, Y.-Q. Zhang and J. Tang, Air-Stable Chiral Single-Molecule Magnets with Record Anisotropy Barrier Exceeding 1800 K, *J. Am. Chem. Soc.*, 2021, **143**, 10077–10082.

54 W.-J. Xu, Q.-C. Luo, Z.-H. Li, Y.-Q. Zhai and Y.-Z. Zheng, Bis-Alkoxide Dysprosium(III) Crown Ether Complexes Exhibit Tunable Air Stability and Record Energy Barrier, *Adv. Sci.*, 2024, **11**, 2308548.

55 Y.-C. Chen, J.-L. Liu, L. Ungur, J. Liu, Q.-W. Li, L.-F. Wang, Z.-P. Ni, L. F. Chibotaru, X.-M. Chen and M.-L. Tong, Symmetry-Supported Magnetic Blocking at 20 K in Pentagonal Bipyramidal Dy(III) Single-Ion Magnets, *J. Am. Chem. Soc.*, 2016, **138**, 2829–2837.

56 J. Liu, Y.-C. Chen, J.-L. Liu, V. Vieru, L. Ungur, J.-H. Jia, L. F. Chibotaru, Y. Lan, W. Wernsdorfer, S. Gao, X.-M. Chen and M.-L. Tong, A Stable Pentagonal Bipyramidal Dy(III) Single-Ion Magnet with a Record Magnetization Reversal Barrier over 1000 K, *J. Am. Chem. Soc.*, 2016, **138**, 5441–5450.

57 G. Mezei, C. M. Zaleski and V. L. Pecoraro, Structural and Functional Evolution of Metallacrowns, *Chem. Rev.*, 2007, **107**, 4933–5003.

58 C. M. Zaleski, *Advances in Metallacrown Chemistry*, Springer, 2022.

59 C. M. Zaleski, S. Tricard, E. C. Depperman, W. Wernsdorfer, T. Mallah, M. L. Kirk and V. L. Pecoraro, Single Molecule Magnet Behavior of a Pentanuclear Mn-Based Metallacrown Complex: Solid State and Solution Magnetic Studies, *Inorg. Chem.*, 2011, **50**, 11348–11352.

60 G. A. Bain and J. F. Berry, Diamagnetic Corrections and Pascal's Constants, *J. Chem. Educ.*, 2008, **85**, 532–536.

61 W. Wernsdorfer, Classical and Quantum Magnetization Reversal Studied in Nanometer-Sized Particles and Clusters, *Adv. Chem. Phys.*, 2001, **118**, 99–190.

62 (*a*) I. F. Galván, M. Vacher, A. Alavi, C. Angeli, F. Aquilante, J. Autschbach, J. J. Bao, S. I. Bokarev, N. A. Bogdanov, R. K. Carlson, L. F. Chibotaru, *et al.*, The OpenMolcas *Web*: A Community-Driven Approach to Advancing Computational Chemistry, *J. Chem. Theory Comput.*, 2023,

19, 6933–6991; (*b*) L. F. Chibotaru and L. Ungur, *Ab initio* calculation of anisotropic magnetic properties of complexes. I. Unique definition of pseudospin Hamiltonians and their derivation, *J. Chem. Phys.*, 2012, **137**, 064112.

63 K. Pierloot, in *Computational Organometallic Chemistry*, ed. T. R. Cundari, Marcel Dekker Inc., New York, 2001, pp. 123–158.

64 (*a*) F. Neese, Software Update: The ORCA Program System—Version 6.0, *Wiley Interdiscip. Rev.: Comput. Mol. Sci.*, 2025, **15**, e70019; (*b*) F. Neese, Calculation of the zero-field splitting tensor on the basis of hybrid density functional and Hartree-Fock theory, *J. Chem. Phys.*, 2007, **127**, 164112.

65 A. A. Alaimo, E. S. Koumousi, L. Cunha-Silva, L. J. McCormick, S. J. Teat, V. Psycharis, C. P. Raptopoulou, S. Mukherjee, C. Li, S. Das Gupta, A. Escuer, G. Christou and Th. C. Stamatatos, Structural Diversities in Heterometallic Mn-Ca Cluster Chemistry from the Use of Salicylhydroxamic Acid: $\{MnIII_4Ca_2\}$, $\{MnII/III_6Ca_2\}$, $\{MnIII/IV_8Ca\}$, and $\{MnIII_8Ca_2\}$ Complexes with Relevance to Both High and Low-Valent States of the Oxygen-Evolving Complex, *Inorg. Chem.*, 2017, **56**, 10760–10774.

66 A. A. Alaimo, D. Takahashi, L. Cunha-Silva, G. Christou and Th. C. Stamatatos, Emissive $\{Mn_4IIICa\}$ Clusters with Square Pyramidal Topologies: Syntheses and Structural, Spectroscopic, and Physicochemical Characterization, *Inorg. Chem.*, 2015, **54**, 2137–2151.

67 E. S. Koumousi, S. Mukherjee, C. M. Beavers, S. J. Teat, G. Christou and Th. C. Stamatatos, Towards models of the oxygen-evolving complex (OEC) of photosystem II: a Mn_4Ca cluster of relevance to low oxidation states of the OEC, *Chem. Commun.*, 2011, **47**, 11128–11130.

68 P. Happ, C. Plenk and E. Rentschler, 12-MC-4 metallacrowns as versatile tools for SMM research, *Coord. Chem. Rev.*, 2015, **289–290**, 238–260.

69 C. C. Stoumpos, Th. C. Stamatatos, H. Sartzi, O. Roubeau, A. J. Tasiopoulos, V. Nastopoulos, S. J. Teat, G. Christou and S. P. Perlepes, Employment of methyl 2-pyridyl ketone oxime in manganese non-carboxylate chemistry: $MnII_2MnIV$ and $MnII_2MnIII_6$ complexes, *Dalton Trans.*, 2009, 1004–1015.

70 W. Liu and H. H. Thorp, Bond valence sum analysis of metal-ligand bond lengths in metalloenzymes and model complexes. 2. Refined distances and other enzymes, *Inorg. Chem.*, 1993, **32**, 4102–4105.

71 M. Llunell, D. Casanova, J. Girera, P. Alemany and S. Alvarez, *SHAPE, Continuous Shape Measures Calculation; Version 2.0*, Universitat de Barcelona, Barcelona, Spain, 2010.

72 J. M. Clemente-Juan, E. Coronado and A. Gaita-Ariño, Magnetic polyoxometalates: from molecular magnetism to molecular spintronics and quantum computing, *Chem. Soc. Rev.*, 2012, **41**, 7464–7478.

73 A. W. Addison, T. N. Rao, J. Reedijk, J. van Rijn and G. C. Verschoor, Synthesis, structure, and spectroscopic properties of copper(II) compounds containing nitrogen-sulphur donor ligands; the crystal and molecular structure of aqua[1,7-bis(N-methylbenzimidazol-2′-yl)-2,6-dithiaheptane]copper(II) perchlorate, *J. Chem. Soc., Dalton Trans.*, 1984, 1349–1356.

74 I. Nemec, R. Herchel and Z. Trávníček, Pentacoordinate and Hexacoordinate Mn(III) Complexes of Tetradentate Schiff-Base Ligands Containing Tetracyanidoplatinate(II) Bridges and Revealing Uniaxial Magnetic Anisotropy, *Molecules*, 2016, **21**, 1681.

75 R. Maurice, C. de Graaf and N. Guihéry, Magnetostructural relations from a combined ab initio and ligand field analysis for the nonintuitive zero-field splitting in Mn(III) complexes, *J. Chem. Phys.*, 2010, **133**, 084307.

76 E. R. Davidson, *MAGNET*, Indiana University, Bloomington, Indiana, 1999.

77 W. Wernsdorfer, Classical and quantum magnetization reversal studied in nanometer-sized particles and clusters, *Adv. Chem. Phys.*, 2001, **118**, 99–192.

78 T. N. Nguyen, W. Wernsdorfer, K. A. Abboud and G. Christou, A Supramolecular Aggregate of Four Exchange-Biased Single-Molecule Magnets, *J. Am. Chem. Soc.*, 2011, **133**, 20688–20691.

79 C. Rajnák, J. Titiš, J. Moncol, R. Mičová and R. Boča, Field-Induced Slow Magnetic Relaxation in a Mononuclear Manganese(II) Complex, *Inorg. Chem.*, 2019, **58**, 991–994.

80 T. T. da Cunha, V. M. M. Barbosa, W. X. C. Oliveira, E. F. Pedroso, D. M. A. García, W. C. Nunes and C. L. M. Pereira, Field-Induced Slow Magnetic Relaxation of a Six-Coordinate Mononuclear Manganese(II) and Cobalt(II) Oxamate Complexes, *Inorg. Chem.*, 2020, **59**, 12983–12987.

81 K. Uchida, G. Cosquer, K. Sugisaki, H. Matsuoka, K. Sato, B. K. Breedlove and M. Yamashita, Isostructural M(II) complexes (M = Mn, Fe, Co) with field-induced slow magnetic relaxation for Mn and Co complexes, *Dalton Trans.*, 2019, **48**, 12023–12030.

82 L. Ungur and L. F. Chibotaru, Magnetic anisotropy in the excited states of low symmetry lanthanide complexes, *Phys. Chem. Chem. Phys.*, 2011, **13**, 20086–20090.

83 L. F. Chibotaru, L. Ungur, C. Aronica, H. Elmoll, G. Pilet and D. Luneau, Structure, Magnetism, and Theoretical Study of a Mixed-Valence $CoII_3CoIII_4$ Heptanuclear Wheel: Lack of SMM Behavior despite Negative Magnetic Anisotropy, *J. Am. Chem. Soc.*, 2008, **130**, 12445–12455.

84 A. Bencini and D. Gatteschi, *EPR of Exchange Coupled Systems*, Springer, Berlin, 1990.

85 L. Ungur, M. Thewissen, J. P. Costes, W. Wernsdorfer and L. F. Chibotaru, Interplay of strongly anisotropic metal ions in magnetic blocking of complexes, *Inorg. Chem.*, 2013, **52**, 6328–6337.

86 V. Vieru, T. D. Pasatoiu, L. Ungur, E. Suturina, A. M. Madalan, C. Duhayon, J.-P. Sutter, M. Andruh and L. F. Chibotaru, Synthesis, crystal structures, and theoretical investigation of a new series of NiII-LnIII-WV heterotrimetallics: Understanding the SMM behavior of mixed polynuclear complexes, *Inorg. Chem.*, 2016, **55**, 12158–12171.

87 *CrystalClear*, Rigaku/MSC Inc., The Woodlands, TX, 2005.
88 G. M. Sheldrick, A Short History of SHELX, *Acta Crystallogr., Sect. A: Found. Crystallogr.*, 2008, **64**, 112–122.
89 (*a*) G. M. Sheldrick, Crystal structure refinement with SHELXL, *Acta Crystallogr., Sect. C: Struct. Chem.*, 2015, **71**, 3–8; (*b*) A. L. Spek, *PLATON* SQUEEZE: a tool for the calculation of the disordered solvent contribution to the calculated structure factors, *Acta Crystallogr., Sect. C: Struct. Chem.*, 2015, **71**, 9–18.
90 (*a*) K. Brandenburg, *DIAMOND, Release 3.1f*, Crystal Impact GbR, Bonn, Germany, 2008; (*b*) I. J. Bruno, J. C. Cole, P. R. Edgington, M. K. Kessler, C. F. Macrae, P. McCabe, J. Pearson and R. Taylor, New Software for Searching the Cambridge Structural Database and Visualizing Crystal Structures, *Acta Crystallogr., Sect. B: Struct. Sci.*, 2002, **58**, 389.
91 CCDC 2535214: Experimental Crystal Structure Determination, 2026, DOI: **10.5517/ccdc.csd.cc2r3333**.

